ACS Energy LETTERS

Cite This: ACS Energy Lett. 2019, 4, 2480−2488

http://pubs.acs.org/journal/aelccp

LETTER

Unravelling the Chemistry and Microstructure Evolution of a Cathodic Interface in Sulfide-Based All-Solid-State Li-Ion Batteries

Xia Li,[†] Zhouhong Ren,[‡] Mohammad Norouzi Banis,[†] Sixu Deng,[†] Yang Zhao,[†] Qian Sun,[†] Changhong Wang,[†] Xiaofei Yang,[†] Weihan Li,[†,∥] Jianwen Liang,[†] Xiaona Li,[†] Yipeng Sun,[†,∥] Keegan Adair,[†] Ruying Li,[†] Yongfeng Hu,[§] Tsun-Kong Sham,[∥] Huan Huang,[⊥] Li Zhang,[#] Shigang Lu,[#] Jun Luo,*[,‡] and Xueliang Sun*[,†]

[†]Department of Mechanical and Materials Engineering, University of Western Ontario, London, Ontario N6A 5B9, Canada

[‡]Center for Electron Microscopy and Tianjin Key Lab of Advanced Functional Porous Materials, Institute for New Energy Materials and Low-Carbon Technologies, School of Materials Science and Engineering, Tianjin University of Technology, Tianjin 300384, China

[§]Canadian Light Source, 44 Innovation Boulevard, Saskatoon, Saskatchewan S7N 2V3, Canada

[∥]Department of Chemistry, University of Western Ontario, London, Ontario N6A 5B9, Canada

[⊥]Glabat Solid-State Battery Inc., 700 Collip Circle, London, Ontario N6G 4X8, Canada

[#]China Automotive Battery Research Institute Co. Ltd., Fifth Floor, No. 43, Mining Building, North Sanhuan Middle Road, Beijing 100088, China

Supporting Information

ABSTRACT: All-solid-state lithium-ion batteries (SSLIBs) are promising candidates to meet the requirement of electric vehicles due to the intrinsic safety characteristics and high theoretical energy density. A stable cathodic interface is critical for maximizing the performance of SSLIBs. In this study, operando X-ray absorption near-edge spectroscopy (XANES) combined with transmission electron microscopy (TEM) and electron energy loss spectroscopy (EELS) is employed to investigate the interfacial behavior between the Ni-rich layered cathodes and sulfide solid-state electrolyte. The study demonstrates a metastable intermediate state of sulfide electrolyte at high voltage and parasitic reactions with cathodes during the charge/discharge process, which leads to the surface structural reconstruction of Ni-rich cathodes. Constructing a uniform interlayer by atomic layer deposition (ALD) is also employed in this study to further investigate the cathodic interface stability. These results provide new insight into the cathodic interface reaction mechanism and highlight the importance of advanced operando characterizations for SSLIBs.

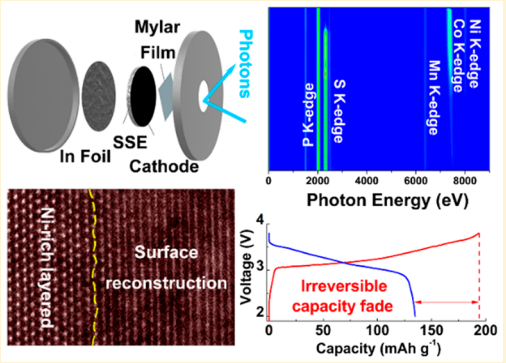

Li-ion batteries (LIBs) have played an essential role in the portable electronic device market and are considered promising candidates as energy storage devices for electric vehicle applications.[1−3] However, the popular organic liquid electrolytes raise serious concerns due to their flammable and toxic properties.[4,5] Fortunately, the replacement of liquid with highly conductive solid-state electrolytes (SSEs) may address these issues.[6−8] Therefore, the development of all-solid-state lithium ion batteries (SSLIBs) has aroused widespread interests due to their intrinsic safety features that circumvent the use of the flammable and toxic organic liquid electrolytes.[9] Furthermore, SSLIBs are proposed to have the potential to compete or even go beyond the energy density of liquid-based LIBs.[10,11] Among the developed SSEs, sulfide-based inorganic SSEs, in particular, have demonstrated high ionic conductivity (10^{-2}−10^{-4} S cm^{-1}), which is almost comparable with that of liquid-based Li-ion electrolytes.[12−15] However, the state-of-the-art SSLIBs with sulfide-based SSEs still suffer from severe issues, such as limited cycle life and rapid performance degradation, which are largely related to the unstable interface between electrode

Received: August 4, 2019
Accepted: September 16, 2019
Published: September 16, 2019

DOI: 10.1021/acsenergylett.9b01676
ACS Energy Lett. 2019, 4, 2480−2488

materials and SSEs that are detrimental to Li-ion transport.[16] Some studies have reported interfacial phenomena between lithium metal oxide cathode materials and sulfide-based electrolytes, such as the space charge effect, the diffusion of transition metals into SSEs, the decomposition of sulfide SSEs to form the inactive interlayer, etc.[17−22] To suppress the side reactions and stabilize the cathode/SSE interface, various coating materials, such as SSE coatings ($Li_2S-P_2S_5$), inactive coatings (Al_2O_3, Li_2CO_3), and ionic conductive coatings ($LiNbO_3$, Li_3PO_4, $LiTaO_3$), have been developed for Li-ion cathodes to improve the electrochemical performance of sulfide-based SSLIBs.[23−27]

Although some reaction mechanisms are proposed, most of the reported studies employed ex situ characterizations to analyze the cathode/SSE interface before and after the electrochemical test.[17,18,28,29] It should be noted that the sulfide SSEs are highly moisture- and air-sensitive, and therefore, postcharacterizations have many challenges to directly reflect the reaction process. Therefore, the underlying mechanisms of sulfide SSEs, such as when and how the side reaction occurs, if there are metastable intermediate phases that existed, are not fully understood. Furthermore, considering the employed cathode materials in SSLIBs, many reaction mechanisms and the structural evolution, such as how the surface structure reconstruction and inner cracking evolve during an electrochemical process and how the developed coating materials work for cathodes to alleviate the side reactions and stabilize the cathode/SSEs interface, should also be further investigated. These unrevealed fundamental studies may impede the design of highly stable and conductive SSE/cathode interfaces and also hinder the development of high-performance SSLIBs.

X-ray absorption near-edge spectroscopy (XANES) has been widely employed in liquid-based LIBs to provide information on the chemical state and local electronic structure of battery materials.[30−32] In particular, advanced operando XANES study, which is a well-known powerful analytic technique to monitor the active intermediate products and reveal the electrochemical reaction mechanism, is used to probe the battery materials while the cell is undergoing electrochemical cycling.[33,34] In this study, operando XANES combined with scanning transmission electron microscopy (STEM) with high-angle annular dark field (HAADF) and electron energy loss spectroscopy (EELS) is carried out to investigate the interface evolution between cathodes and sulfide SSEs in SSLIBs during the charge/discharge process. A commercial Ni-rich layered oxide $LiNi_{0.8}Mn_{0.1}Co_{0.1}O_2$ (NMC811) cathode and $Li_{10}GeP_2S_{12}$ (LGPS) SSE are employed in this study. To investigate the coating strategy for cathodes in SSLIBs, atomic layer deposited (ALD) lithium niobium oxide ($LiNbO_x$) with a controllable and ultrathin thickness is applied as the coating layer for NMC811, which is proposed to stabilize the interface and improve the electrochemical performance of SSLIBs. The comparisons of the bare and coated NMC811 cathodes with electrochemical testing and physicochemical characterizations reveal the interfacial chemistry and microstructure evolution between cathodes and sulfide SSEs during the electrochemical reactions. The study illustrates the instability of LGPS as well as the parasitic reactions with bare NMC811 during the charging process and byproduct Li_2S formation afterward. Furthermore, the surficial structure reconstruction and microstructure cracks of the Ni-rich layered cathode in sulfide solid-state batteries are also investigated. This work highlights that the complete operando XANES analysis combined with TEM provides a detailed scenario of the interface side reactions and, more importantly, presents the experimental value of operando characterizations in the study of SSLIBs.

Figure 1 illustrates the morphology and fine structure of the bare and ALD $LiNbO_x$-coated NMC811 (LNO-NMC811). In

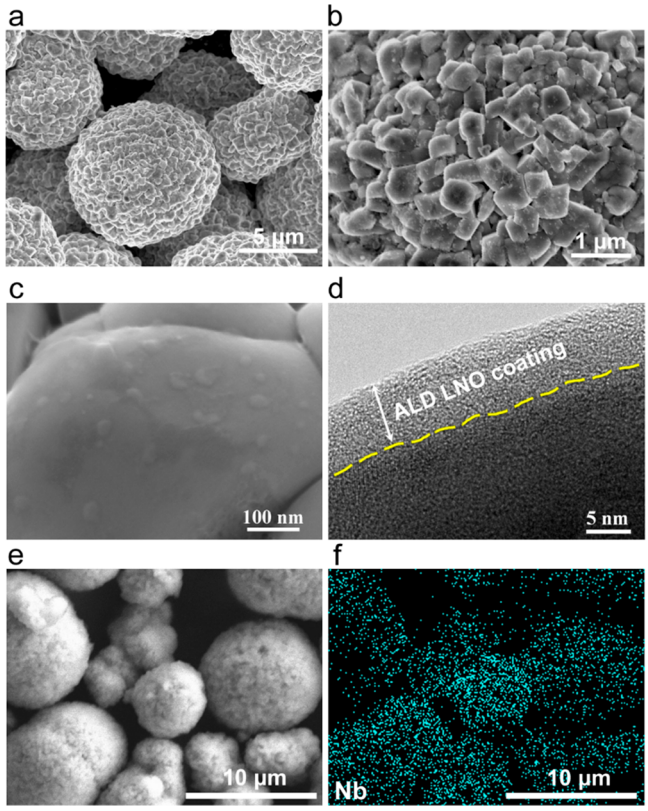

Figure 1. Physical characterizations of bare and LNO-coated NMC811 composites. (a,b) SEM image of bare NMC811. (c) SEM image, (d) HRTEM image, and (e,f) SEM-EDX element mapping of ALD LNO-coated NMC811.

this study, we employ an LNO thin film via ALD as a coating material for Ni-rich cathodes. In our previous study, the ALD LNO thin film demonstrated an acceptable ionic conductivity (6×10^{-8} S cm^{-1}) at room temperature as well as conformal growth and controllable thickness during deposition, which is promising as an interfacial engineering material in solid-state batteries.[35] To investigate the thickness effect, 2, 5, and 10 nm of LNO are deposited on NMC811 cathodes by controlling the ALD reaction cycles (10, 25, and 50 cycles). As shown in Figure 1a,b, commercial NMC811 cathodes are secondary sphere particles with a size of approximately 5−10 μm. After 25 cycles of ALD coating, the surface of the cathode particle appears rougher (Figure 1c), and an amorphous and conformal coating with the thickness of around 5 nm can be observed at the surface of NMC811 (Figure 1d). The deposition thickness corresponds well with the reported linear growth rate at around 0.2 nm per cycle of ALD LNO thin films.[35] Elemental mapping of scanning electron microscopy-energy dispersive X-ray spectrometry (SEM-EDX) shown in Figure 1e,f demonstrates the uniform distribution of Nb element among the NMC811 particles, further confirming the success of LNO coating on cathodes. X-ray diffraction (XRD) and XANES are conducted to evaluate the crystal and chemical structure of

DOI: 10.1021/acsenergylett.9b01676
ACS Energy Lett. 2019, 4, 2480−2488

bare and LNO-coated NMC811 composites. As shown in Figure S1, there are no obvious differences of NMC811 before and after LNO coating, indicating that the material properties are maintained throughout the ALD process and no new impurities are introduced.

The bare and coated NMC811 composites were then mixed with LGPS as cathode materials and assembled in SSLIBs. SEM images of the top view of the pressed NMC811-LGPS pellet are shown in Figure S2, and the detailed SSLIB assembly process is listed in the Experimental Section. Electrochemical impedance spectroscopy (EIS) plots of LGPS at various temperatures are presented in Figure S3. Fitting the conductivities derived from the temperature-dependent impedance with an Arrhenius law results in ionic conductivity of 2.07×10^{-3} S cm^{-1} for the commercial LGPS at room temperature, which is similar to the reported values.[19,36−38] Electrochemical characterizations of assembled SSLIBs are shown in Figures 2 and S4. The thickness effect of the LNO coating layer for the performance of NMC811 cathodes is first optimized in Figure S4, and 5 nm of LNO-NMC811 presents the best electrochemical performance. Comparing the charge/discharge profiles, the bare NMC811 demonstrates a significantly irreversible capacity at the first cycle with a low Coulombic efficiency of 65%. In addition, there is a slight slope circled in Figure 2a at the initial charging process, corresponding to the space charge effect reported by previous studies.[12,39] Furthermore, the bare NMC811 shows that severe voltage plateaus fade in the following cycles and the capacity drops rapidly. On the other hand, among the coated cathodes, 5 nm of LNO-NMC811 demonstrates significantly improved electrochemical performance. The initial charge stage does not exhibit the same sloping voltage profile as the bare NMC811, indicating that the LNO coating effectively prevents the occurrence of space charge behavior. Furthermore, the irreversible capacity of the first cycle is significantly reduced, and the Coulombic efficiency exceeds 82%. The cycling performance of the as-prepared cathodes is shown in Figures 2c and S4. Compared with the bare and LNO-coated NMC811 cathodes with the different thicknesses of LNO coating layers, 5 nm of LNO-NMC811 demonstrates significantly improved cycling capacity and stability. After 50 cycles, the discharge capacity remains at 99 mAh g^{-1}, while the discharge capacity of the bare NMC811 is only 20 mAh g^{-1}. The differences of the electrochemical performance are primarily related to the interface resistance between the cathode and sulfide electrolyte. The charge transfer resistance, including both Li-ion transportation and electron conduction resistance, is one of the factors that affects the electrochemical performance of SSLIBs.[11] More importantly, the side reactions between sulfide SSEs and cathodes result in the large resistance at the interface with the decomposition of SSEs during cycling.[12,17] Therefore, constructing the coating layer with an appropriate thickness for cathodes is a necessary step to suppress the side reactions with sulfide SSEs and achieve the good electrochemical performance. EIS measurement is conducted to evaluate the resistance of as-assembled batteries, as shown in Figure 2d,e. Before electrochemical cycling, the two batteries after assembly demonstrate small surface charge transfer resistances, indicating good conductivity at the cathode/SSE interface. However, after 10 h of rest, the two batteries appear to have differences in the EIS plots. The semicircle at the high-frequency region of the bare NMC811-LGPS battery becomes significantly larger, indicating an increased resistance during the resting period. Furthermore, after one charge/discharge cycle and 2 h of rest, the resistance of the battery with bare NMC811 increases more obviously, which is indicative of the unstable interface between the bare Ni-rich cathode and LGPS during cycling. In order to investigate the interfacial stability between the In anode and LGPS SSEs, the EIS plots and CV curves of In-LGPS-In battery are shown in Figure S5. After several hours of rest, the EIS plots of the In-LGPS-In battery are almost not changed. For the CV test, no obvious anodic peak can be observed during the scanning process, indicating the stable anodic interface during electrochemical reactions.

The electrochemical characterizations have provided evidence of the side reactions between bare NMC811 and LGPS and demonstrated the different interfacial behavior between the bare and coated NMC811 with LGPS. To further reveal the interface chemistry, ex situ and *operando* XANES studies were conducted. Figure S6a,b illustrates the ex situ XANES of cathodes and SSEs before battery assembly. Interestingly, just

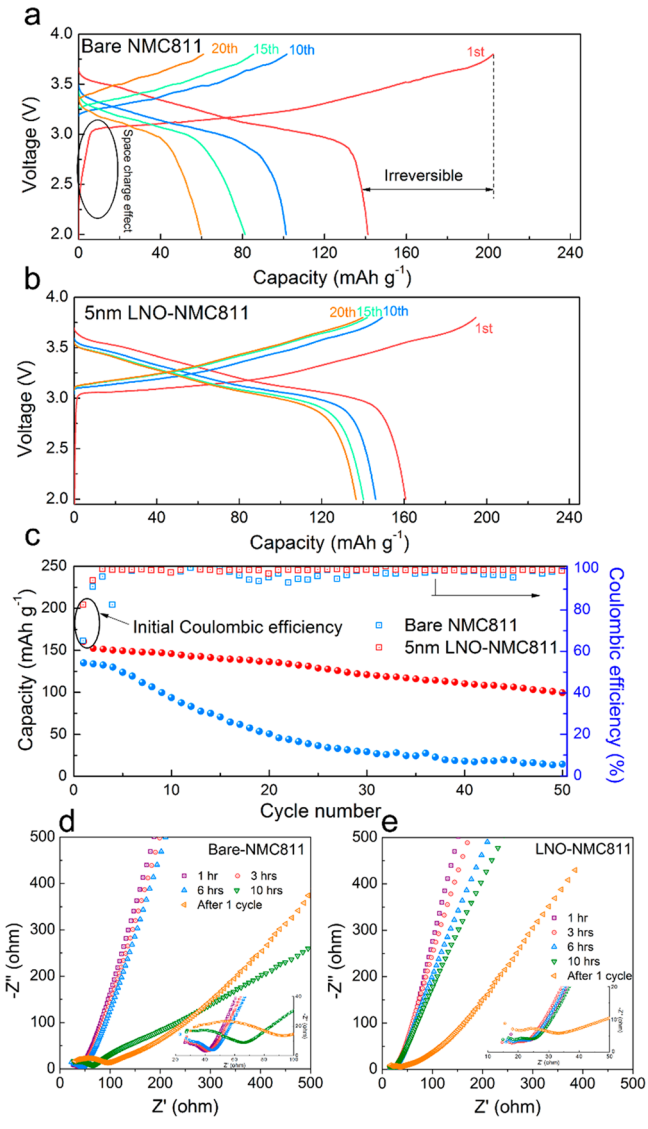

Figure 2. Electrochemical characterizations of bare and LNO-coated NMC811 in SSLIBs. (a,b) Charge/discharge profiles, (c) cycling performance, and (d,e) EIS plots of batteries at a various resting times and after the charge/discharge test.

DOI: 10.1021/acsenergylett.9b01676
ACS Energy Lett. 2019, 4, 2480−2488

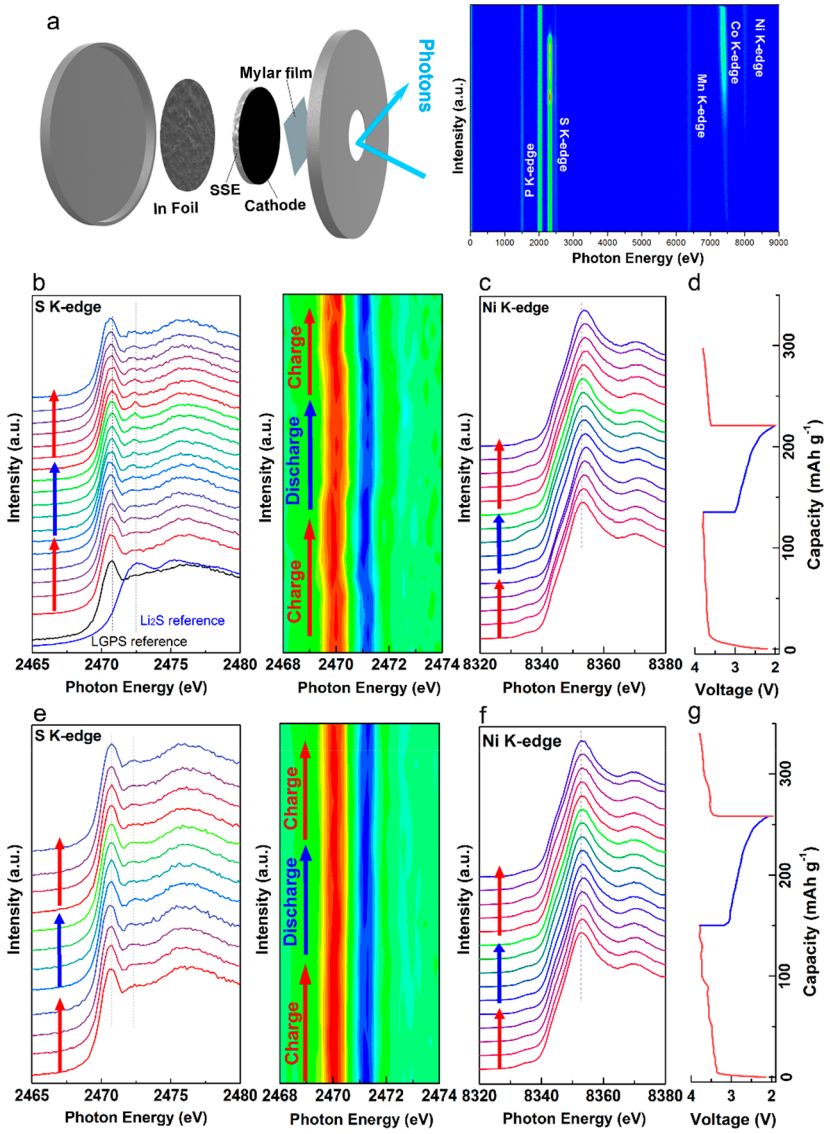

Figure 3. Operando XANES study of SSLIBs with bare and LNO-coated NMC811 cathodes during cycling: (a) schematic figure of the operando cell and obtained Bruker spectrum in a large photon energy region. Operando S K-edge spectra with first derivative mapping, Ni K-edge spectra, and charge/discharge profiles of (b−d) bare NMC811-LGPS and (e−g) LNO NMC811-LGPS SSLIBs.

after the bare NMC811 and LGPS composites mixed and rested over 72 h, the feature at 2470.7 eV of the S K-edge presented a shift in the edge jump from 2469.9 to 2470.2 eV, while the feature at 8353 eV of the Ni K-edge shifted to lower energy (8352.2 eV), which is indicative of some interaction between LGPS and NMC811. When the sulfide SSEs and cathodes contact each other, the Li elements from sulfide SSEs prefer to be attracted by lithium metal oxide cathodes, leading to reduced Li concentration in the SSEs and new interlayer formation. This phenomenon is called space charge effect, corresponding to the slope at the initial charging process.[12,39,40] Furthermore, the interdiffusion of transition metals from cathodes and sulfur from SSEs leads to the decomposition of battery materials and formation of insulated interphases.[29,41,42] All of these side reactions result in the changes of the chemical state and local environments of LGPS and NMC811, corresponding to the energy shift of the features in the S and Ni K-edge spectra. On the other hand, with the protection of the coating layer, the NMC811 and LGPS mixture at the same conditions is very stable without obvious changes from the XANES results, indicating that the coating layer enhances the chemical stability of the interface between the cathode and sulfide SSEs. After the charge/discharge cycling test, as shown in Figure S6c,d, the feature at 2470.7 eV in the S K-edge spectrum of bare the NMC-LGPS system becomes very broad and shifts to higher energy, indicating the decomposition of LGPS with bare NMC811 during cycling. Furthermore, the Ni K-edge spectra of both bare and coated NMC811 are shifted to higher energy after a long time cycling, indicating the irreversible chemical state change of the Ni element of NMC811 in SSLIBs. However, due to the inherent feature of ex situ characterization, the detailed reaction manner, such as when, where, and how the interfacial side reactions proceed, is still unknown.

To overcome the limitation of ex situ characterizations, operando XANES was conducted with real-time measurements of the batteries during electrochemical cycling. A modified coin cell configuration was utilized as the operando cell with an opened window that allowed the incident X-rays to penetrate through, as shown in Figure 3a. It should be noticed that the

DOI: 10.1021/acsenergylett.9b01676
ACS Energy Lett. 2019, 4, 2480−2488

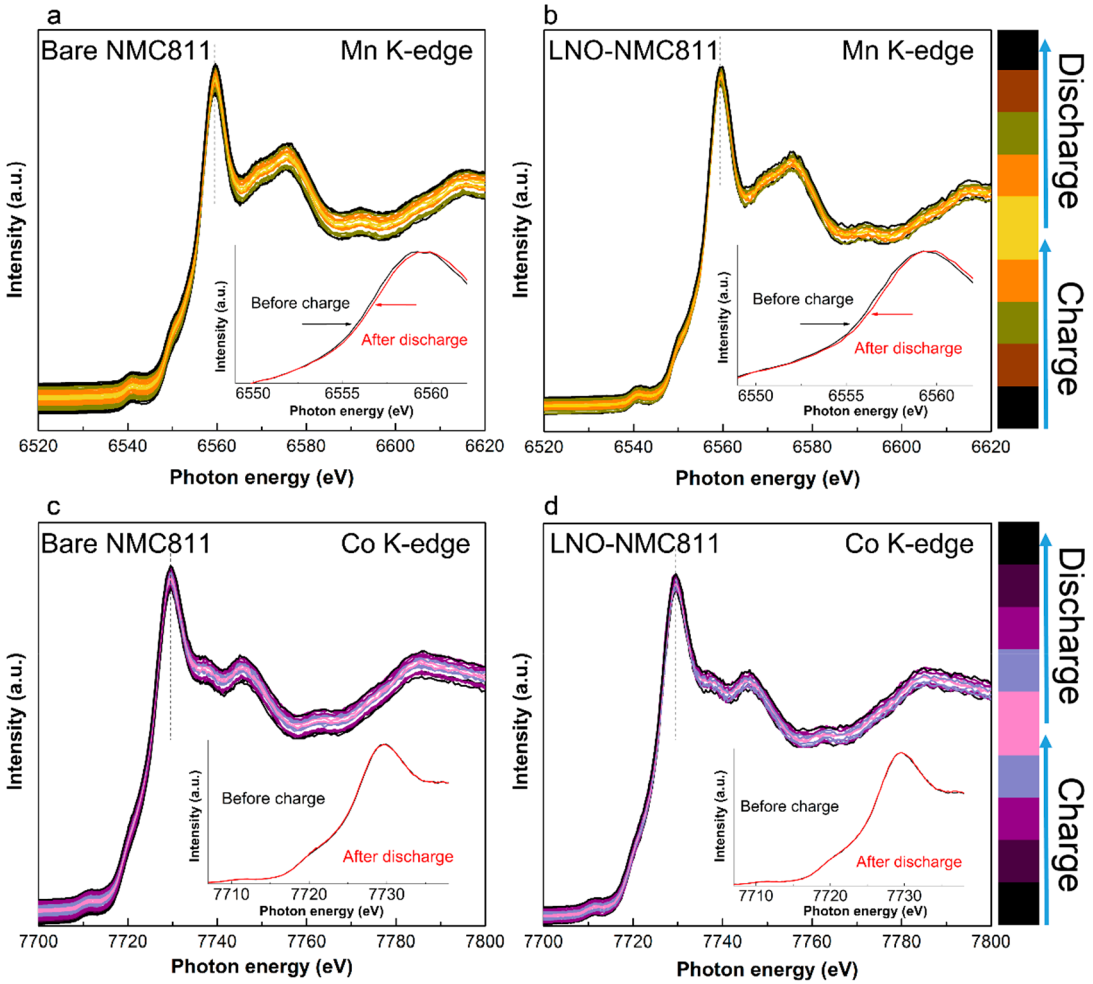

Figure 4. Operando XANES spectra of transition metals of bare and LNO-coated NMC811 cathodes. (a,c) Mn and Co K-edge spectra of bare NMC; (b,d) Mn and Co K-edge spectra of LNO-NMC811.

structure of the operando cell is different from that of the model cell, which is adopted for electrochemical tests (Figure S7). The operando XANES proceeded in a full and half cycle (charge/discharge/charge) of batteries during electrochemical cycling. The obtained results of the bare NMC811-LGPS battery are listed in Figure 3b–d, consisting of the S K-edge spectra with first derivative mapping (Figure 3b), Ni K-edge spectra (Figure 3c), and charge/discharge/charge profiles (Figure 3d). The corresponding results of LNO-NMC811-LGPS SSLIB are listed in Figure 3e–g. First, Ni K-edge spectra of both bare and coated cathodes demonstrate similar evolution during the cycling process. As shown in Figure 3c,g, the spectrum presents a white line at 8353 eV, corresponding to the 1s to 4p transition.[43,44] During the charge/discharge process, the feature at 8353 eV initially shifts to higher energy and then returns back, indicating the Ni^{2+}/Ni^{3+} and Ni^{3+}/Ni^{4+} electrochemical redox reaction in the delithiation/lithiation process of NMC811.[1,3,45] The corresponding Ni K-edge first derivation spectra in Figure S8 further substantiate the evolution. Second, the interpretation of the S K-edge spectral features in this system is much more complicated. The S K-edge white line of LGPS with bare NMC811 is at 2470.7 eV (Figure 3b). During the first charging process, this feature gradually shifts to lower energy. When charging at the high-voltage stage (>3.5 V), the feature shifts from 2470.7 to 2470.4 eV, indicating the instability of LGPS. Furthermore, during the subsequent discharge process, the shifted feature reverses back to 2470.7 eV gradually, while a new feature at 2472.5 eV becomes more prominent. Compared to the standard reference samples (Figure S9), the appearance of the new peak can be assigned to the S 1s to Li_2S σ^* transition,[46] indicating that LGPS is first decomposed to Li_2S rather than metal sulfides or polysulfide. The whole process is repeatable that the feature at 2470.7 eV in the second charging process shifts to lower energy again. The first derivative mapping of the S K-edge spectra gives more direct observation of the evolution, in which the bright red and blue regions present a consistent shift and skew in the image. On the other hand, the S K-edge spectra of LGPS with LNO-NMC811 are very stable during the whole electrochemical reaction and do not show the obvious shift in features during the electrochemical reaction processes. When comparing the first derivative mappings of the two S K-edge spectra, the bright red and blue regions of the LNO-NMC811-LGPS battery are very straight, which is indicative of the stabilized interface between LGPS and the protected cathode during the first charge/discharge/charge process. It should be noted that the developed coin-cell configuration with an open window induces potential polarization of SSLIBs. The discharge voltage plateaus measured in operando study are lower than regular charge/discharge characterizations, which needs further advancements in solid-state cell configuration for operando

DOI: 10.1021/acsenergylett.9b01676
ACS Energy Lett. 2019, 4, 2480–2488

XANES studies. Apart from the S and Ni K-edge spectra, studies of transition metal Mn and Co K-edge spectra are also conducted in the operando XANES characterization, as shown in Figure 4. The Mn K-edge spectrum exhibits the pre-edge at around 6541 eV and the white line at 6559 eV. During the charge/discharge process, the peaks at 6559 eV of both bare and coated NMC (Figure 4a,b) slightly shift to higher energy.[2,43] These shifts are indicative of local environment changes of Mn during the delithiation/lithiation process and related to the structural degradation of the cathode during cycling with LGPS SSE.[1−3,43,47] Compared to the Mn K-edge spectra, the spectra of Co K-edge in both bare and coated NMC811 (Figure 4c,d) do not display obvious shifts, indicating that the Co element from NMC is relatively stable during electrochemical reaction in SSLIBs.

To further understand the microstructure and chemical evolution of cathode materials after cycling, XRD and electron microscopy techniques are utilized to investigate the NMC811 cathodes after charge/discharge cycling. The XRD patterns of bare NMC811 before and after cycling are shown in Figure S10. The evolution of peaks after cycling indicates the structural change of MNC811 during the charge/discharge process. Figures 5 shows the SEM images and corresponding EDX elemental mapping of bare and coated NMC811 after 40 cycles. The cross-sectional SEM specimens were prepared via a focused ion beam (FIB) technique. Interestingly, the intensive intergranular cracks can be detected at the surface of the bare NMC811 spherical secondary particle, as shown in Figure 5a,b. With the continued FIB thinning process, the distinct cracks can be observed at the surface and extend to the interior of the particle, as shown in Figure S11a, suggesting that the cracks originate from the surface and then propagate to the bulk structure of NMC811 during the cycling. SEM-EDX mapping and linear scan spectra in Figures 5c and S12a demonstrate that the sulfur element shows enrichment within the bare NMC811 particle, indicating that the sulfur element is very easy to diffuse into the NMC811 particles and forms an unstable interface during battery operation, inducing the structural evolution and cracks of NMC811 cathodes. On the contrary, the phenomena of both surficial cracks and sulfur element diffusion significantly decline in the LNO-coated NMC811 particle, indicating that the coating layer effectively constructs a protective interface between the cathode and SSEs to maintain the integrity of the cathode particle and suppress the occurrence of side reactions. Figures 6 and S13 are the atomic-level structural images and EELS of cycled bare and LNO-coated NMC811 cathodes, respectively. As shown in Figure 6a, the bare NMC811 after cycling presents obvious differences in the lattice patterns between the surface and bulk region. As confirmed by the inset fast Fourier transformation (FFT) in Figure 6a, the lattice pattern at the near-surface within 12 nm can be indexed as the rock-salt phase with a space group of $Fm\bar{3}m$, while the inner region still maintains the layered structure phase with a space group of $R\bar{3}m$, which is clear evidence that the surface structure of bare NMC811 has been changed and reconstructed during cycling due to the side reactions with sulfide SSEs. EELS spectra further substantiate the significant features of the structural lattice reconstruction. As shown in Figure 6b,c, the O K-edge spectra present suppression of the pre-edge feature from the bulk to surface. The oxygen pre-edge is associated with the transition of electrons from the 1s core state to unoccupied 2p states hybridized with 3d states in transition metals.[48,49] Therefore, a

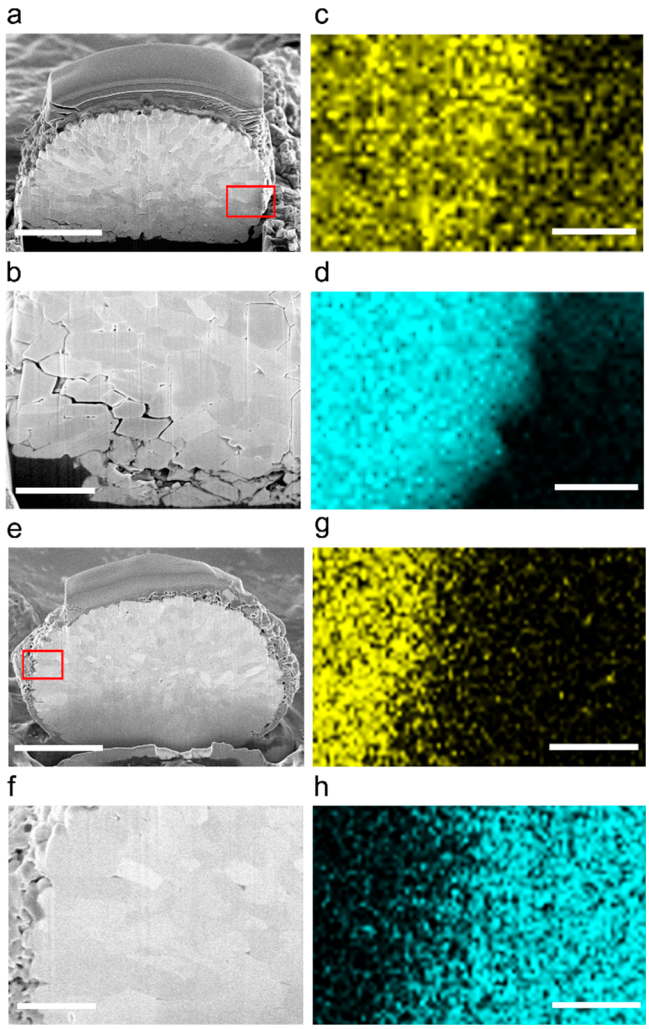

Figure 5. Microstructure evolution of NMC811 cathodes after cycling in SSLIBs identified by SEM images and EDX mapping. (a,b) Cross-sectional FIB-SEM images and (c,d) corresponding S (yellow) and Ni (cyan) maps of the red region in (a) of a bare NMC811 cathode particle. (e,f) Cross-sectional FIB-SEM images and (g,h) corresponding S (yellow) and Ni (cyan) maps of the red region in (e) of an LNO-coated NMC811 cathode particle. Scale bars in the figures are (a,e) 2 μm and (b−d,f−h) 1 μm.

gradual suppression of the oxygen pre-edge indicates the formation of an oxygen vacancy and the reduction of transition metals.[49] Furthermore, the Mn L-edge spectra show that the ratio of the Mn L_3/L_2 feature is increased from the bulk to surface, indicating that Mn reduction is more significant in the rock-salt region.[48,50] The chemical shift of the Ni L-edge is also notable, which indicates the reduction of Ni at the surface region. The surface lattice evolution of NMC cathodes associated with transition metal reduction is widely observed in the liquid-based LIBs, which is mainly derived from the side reactions with electrolyte during the cycling.[51] The atomic-level structural images and EELS spectra in this study confirm that the severe side reaction-induced surface lattice evolution of NMC cathodes also can be observed in the sulfide-based SSBs. Compared to the bare NMC811, the surface phase change of LNO-coated NMC811 is not obvious, as shown in Figure S13. The lattice pattern of the bulk region (black) presents a clear layered structure feature, and the surface region (green) is slightly different from the bulk region,

DOI: 10.1021/acsenergylett.9b01676
ACS Energy Lett. 2019, 4, 2480−2488

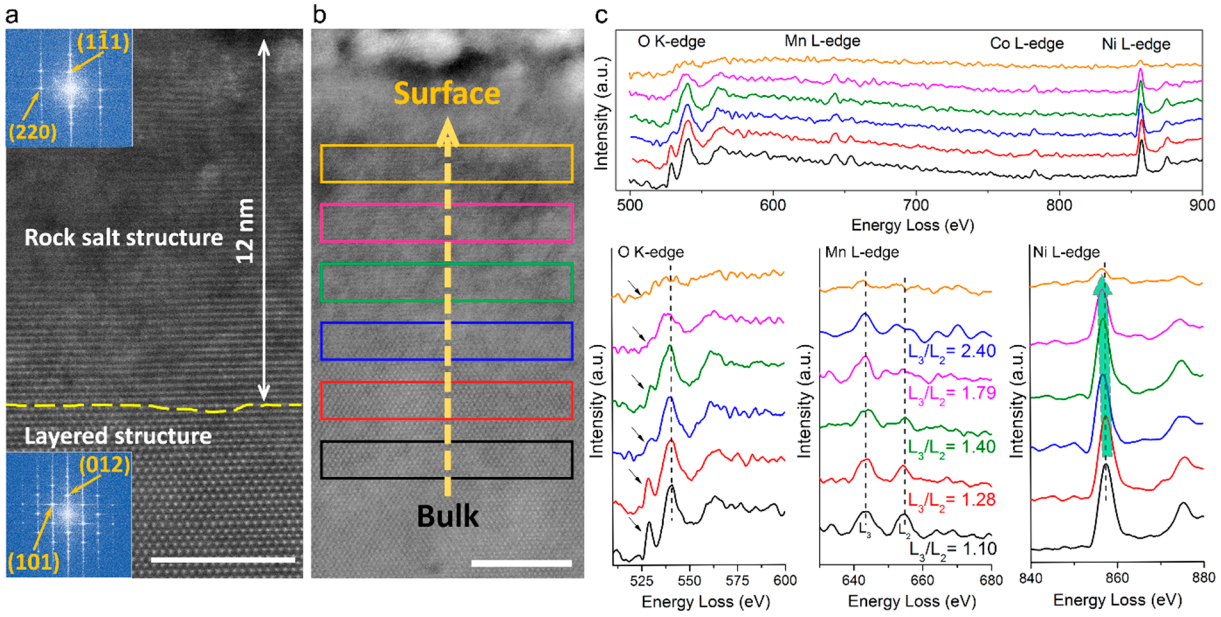

Figure 6. Microstructure evolution of NMC811 cathodes after cycling in SSLIBs identified by STEM-HAADF images and corresponding EELS spectra. (a) Atomic-level STEM-HAADF image of a bare NMC811 cathode after cycling with corresponding FFT patterns inset. (b,c) STEM-HAADF image and corresponding EELS spectra acquired from the regions. Scale bars in the figures are (a,b) 5 nm.

illustrating the change of the layered structure to a disordered structure at the surface region of NMC811 after cycling. The Mn L-edge and O K-edge also present a similar tendency that transition metals are slightly reduced at the surface, which indicates that coating can slow down but still cannot stop the occurrence of side reactions. Therefore, combined with SEM, STEM, and EELS results, it strongly indicated the structural degradation of bare NMC811 cathodes after cycling. The results demonstrate that the severe side reactions with sulfide SSEs not only induce the diffusion of sulfur into the NMC811 particles but also accelerate the formation of microstructural cracks on the surface of NMC811 cathodes. As a result, the transition metal reduction and surface structure reconstruction of NMC811 are undeniable in sulfide-based SSLIBs, leading to poor electrochemical performance of batteries.

Combing operando XANES, STEM, and EELS results, we propose the following interfacial reaction mechanism: the contact of bare NMC811 and LGPS induces parasitic reactions at their interface, which leads to chemical state changes of the cathode and sulfide. During the initial charging process, especially at high voltage, LGPS presents a metastable intermediate state. During the following discharge process, the intermediate state cannot fully reverse back. As a result, some of the LGPSs are first decomposed to form a Li_2S impurity phase. At the same time, the parasitic reactions accelerate the microstructure degradation of NMC811 from the surface to bulk during cycling, leading to the microstructural cracks at the surface of cathode particles, surficial transition metal reduction of cathodes, and phase evolution from the layered to rock-salt structure. The parasitic reactions that occurred at both sulfide SSE and cathode sides are accumulated at the interface gradually and cut off the ionic conductivity, resulting in a large irreversible capacity and fast performance degradation. Coating, on the contrary, helps to protect the integrity of the NMC811 cathode and stabilize the interface between the cathode and sulfide SSEs, leading to promising cycling performance of the cathode in SSLIBs.

In summary, we investigated the chemistry and microstructure evolution at the interface between layered NMC811 cathodes and LGPS sulfide SSEs in SSLIBs via operando XANES and electron microscopy studies. Our results expand the understanding of the interface mechanism of inorganic-based SSLIBs and demonstrate the potential of operando characterization studies to probe the highly reactive intermediate states and unravel the complex reaction mechanisms of energy materials.

■ ASSOCIATED CONTENT

Supporting Information

The Supporting Information is available free of charge on the ACS Publications website at DOI: 10.1021/acsenergylett.9b01676.

Detailed experimental procedures; XRD patterns, XANES spectra, and SEM images of as-prepared cathode composites; additional electrochemical characterizations; schematic figure of the model cell; ex situ and in situ XANES spectra of various cathodes before and after cycling; and SEM images, STEM-HAADF images and corresponding EELS spectra of bare and modified cathodes (PDF)

■ AUTHOR INFORMATION

Corresponding Authors

*E-mail: xsun@eng.uwo.ca (X.S.).
*E-mail: jluo@tjut.edu.cn (J.L.).

ORCID

Mohammad Norouzi Banis: 0000-0002-6144-6837
Jun Luo: 0000-0001-5084-2087
Xueliang Sun: 0000-0003-2881-8237

Author Contributions

Xia Li, Zhouhong Ren, and Mohammad Norouzi Banis contributed equally to this work. Prof. Xueliang Sun supervised the overall project. Xia Li conceived this idea, synthesized the

DOI: 10.1021/acsenergylett.9b01676
ACS Energy Lett. 2019, 4, 2480−2488

electrodes, characterized the samples, tested the electrochemical performances, and wrote this manuscript. Zhouhong Ren and Jun Luo performed the TEM characterization at Tianjin University of Technology. Xia Li, Mohammad Norouzi Banis, Qian Sun, Weihan Li, Jianwen Liang, Yongfeng Hu, and Tsun-Kong Sham carried out the synchrotron radiation characterization at CLS. Sixu Deng, Changhong Wang, Xiaofei Yang, and Xiaona Li performed electrochemical characterization. Yang Zhao and Yipeng Sun performed the ALD process. Keegan Adair polished the language. Ruying Li carried out SEM characterization and purchased all of the chemicals. All of the authors discussed the results and commented on the manuscript. All authors have given approval to the final version of the manuscript.

Notes

The authors declare no competing financial interest.

■ ACKNOWLEDGMENTS

This research was supported by the Natural Sciences and Engineering Research Council of Canada (NSERC), Canada Research Chair Program (CRC), Canada Foundation for Innovation (CFI), Ontario Research Fund (ORF), the Canada Light Source at University of Saskatchewan (CLS), Interdisciplinary Development Initiatives (IDI) by Western University, and University of Western Ontario. Xia Li acknowledges support of the Mitacs Elevate Postdoctoral Fellowship.

■ REFERENCES

(1) Xia, Y.; Zheng, J.; Wang, C.; Gu, M. Designing Principle for Ni-Rich Cathode Materials with High Energy Density for Practical Applications. *Nano Energy* **2018**, *49*, 434−452.

(2) Kim, J.; Lee, H.; Cha, H.; Yoon, M.; Park, M.; Cho, J. Prospect and Reality of Ni-Rich Cathode for Commercialization. *Adv. Energy Mater.* **2018**, *8*, 1702028.

(3) Zeng, X.; Zhan, C.; Lu, J.; Amine, K. Stabilization of a High-Capacity and High-Power Nickel-Based Cathode for Li-Ion Batteries. *Chem.* **2018**, *4*, 690−704.

(4) Xu, K. Electrolytes and Interphases in Li-Ion Batteries and Beyond. *Chem. Rev.* **2014**, *114* (23), 11503−11618.

(5) Doughty, D. H.; Roth, E. P.; Crafts, C. C.; Nagasubramanian, G.; Henriksen, G.; Amine, K. Effects of Additives on Thermal Stability of Li Ion Cells. *J. Power Sources* **2005**, *146*, 116−120.

(6) Kim, J. G.; Son, B.; Mukherjee, S.; Schuppert, N.; Bates, A.; Kwon, O.; Choi, M. J.; Chung, H. Y.; Park, S. A Review of Lithium and Non-Lithium Based Solid State Batteries. *J. Power Sources* **2015**, *282*, 299−322.

(7) Yang, C.; Fu, K.; Zhang, Y.; Hitz, E.; Hu, L. Protected Lithium-Metal Anodes in Batteries: From Liquid to Solid. *Adv. Mater.* **2017**, *29*, 1701169.

(8) Manthiram, A.; Yu, X.; Wang, S. Lithium Battery Chemistries Enabled by Solid-State Electrolytes. *Nat. Rev. Mater.* **2017**, *2*, 16103.

(9) Bachman, J. C.; Muy, S.; Grimaud, A.; Chang, H.-H.; Pour, N.; Lux, S. F.; Paschos, O.; Maglia, F.; Lupart, S.; Lamp, P.; Giordano, L.; Shao-Horn, Y. Inorganic Solid-State Electrolytes for Lithium Batteries: Mechanisms and Properties Governing Ion Conduction. *Chem. Rev.* **2016**, *116*, 140−162.

(10) Quartarone, E.; Mustarelli, P. Electrolytes for Solid-State Lithium Rechargeable Batteries: Recent Advances and Perspectives. *Chem. Soc. Rev.* **2011**, *40*, 2525−2540.

(11) Li, X.; Liang, J.; Li, X.; Wang, C.; Luo, J.; Li, R.; Sun, X. High-Performance All-Solid-State Li-Se Batteries Induced by Sulfide Electrolytes. *Energy Environ. Sci.* **2018**, *11*, 2828−2832.

(12) Wu, B.; Wang, S.; Evans, W. J., IV; Deng, D. Z.; Yang, J.; Xiao, J. Interfacial Behaviours between Lithium Ion Conductors and Electrode Materials in Various Battery Systems. *J. Mater. Chem. A* **2016**, *4*, 15266−15280.

(13) Kato, Y.; Hori, S.; Saito, T.; Suzuki, K.; Hirayama, M.; Mitsui, A.; Yonemura, M.; Iba, H.; Kanno, R. High-Power All-Solid-State Batteries Using Sulfide Superionic Conductors. *Nat. Energy* **2016**, *1*, 16030.

(14) Liu, Z.; Fu, W.; Payzant, E. A.; Yu, X.; Wu, Z.; Dudney, N. J.; Kiggans, J.; Hong, K.; Rondinone, A. J.; Liang, C. Anomalous High Ionic Conductivity of Nanoporous Beta-Li_3PS_4. *J. Am. Chem. Soc.* **2013**, *135*, 975−978.

(15) Rangasamy, E.; Liu, Z.; Gobet, M.; Pilar, K.; Sahu, G.; Zhou, W.; Wu, H.; Greenbaum, S.; Liang, C. An Iodide-Based $Li_7P_2S_8I$ Superionic Conductor. *J. Am. Chem. Soc.* **2015**, *137*, 1384−1387.

(16) Culver, S. P.; Koerver, R.; Zeier, W. G.; Janek, J. On the Functionality of Coatings for Cathode Active Materials in Thiophosphate-Based All-Solid-State Batteries. *Adv. Energy Mater.* **2019**, *9*, 1900626.

(17) Koerver, R.; Aygün, I.; Leichtweiß, T.; Dietrich, C.; Zhang, W.; Binder, J. O.; Hartmann, P.; Zeier, W. G.; Janek, J. Capacity Fade in Solid-State Batteries: Interphase Formation and Chemomechanical Processes in Nickel-Rich Layered Oxide Cathodes and Lithium Thiophosphate Solid Electrolytes. *Chem. Mater.* **2017**, *29*, 5574−5582.

(18) Auvergniot, J.; Cassel, A.; Ledeuil, J.-B.; Viallet, V.; Seznec, V.; Dedryvère, R. Interface Stability of Argyrodite Li_6PS_5Cl toward $LiCoO_2$, $LiNi_{1/3}Co_{1/3}Mn_{1/3}O_2$, and $LiMn_2O_4$ in Bulk All-Solid-State Batteries. *Chem. Mater.* **2017**, *29*, 3883−3890.

(19) Oh, G.; Hirayama, M.; Kwon, O.; Suzuki, K.; Kanno, R. Bulk-Type All Solid-State Batteries with 5 V Class $LiNi_{0.5}Mn_{1.5}O_4$ Cathode and $Li_{10}GeP_2S_{12}$ Solid Electrolyte. *Chem. Mater.* **2016**, *28*, 2634−2640.

(20) Lau, J.; DeBlock, R. H.; Butts, D. M.; Ashby, D. S.; Choi, C. S.; Dunn, B. S. Sulfide Solid Electrolytes for Lithium Battery Applications. *Adv. Energy Mater.* **2018**, *8*, 1800933.

(21) Sumita, M.; Tanaka, Y.; Ikeda, M.; Ohno, T. Charged and Discharged States of Cathode/Sulfide Electrolyte Interfaces in All-Solid-State Lithium Ion Batteries. *J. Phys. Chem. C* **2016**, *120*, 13332−13339.

(22) Sumita, M.; Tanaka, Y.; Ohno, T. Possible Polymerization of PS_4 at a $Li_3PS_4/FePO_4$ Interface with Reduction of the $FePO_4$ Phase. *J. Phys. Chem. C* **2017**, *121*, 9698−9704.

(23) Sakuda, A.; Hayashi, A.; Ohtomo, T.; Hama, S.; Tatsumisago, M. All-Solid-State Lithium Secondary Batteries Using $LiCoO_2$ Particles with Pulsed Laser Deposition Coatings of Li_2S-P_2S_5 Solid Electrolytes. *J. Power Sources* **2011**, *196*, 6735−6741.

(24) Takada, K.; Ohta, N.; Zhang, L.; Fukuda, K.; Sakaguchi, I.; Ma, R.; Osada, M.; Sasaki, T. Interfacial Modification for High-Power Solid-State Lithium Batteries. *Solid State Ionics* **2008**, *179*, 1333−1337.

(25) Ito, Y.; Sakurai, Y.; Yubuchi, S.; Sakuda, A.; Hayashi, A.; Tatsumisago, M. Application of $LiCoO_2$ Particles Coated with Lithium Ortho-Oxosalt Thin Films to Sulfide-Type All-Solid-State Lithium Batteries. *J. Electrochem. Soc.* **2015**, *162*, A1610−A1616.

(26) Kim, J.; Kim, M.; Noh, S.; Lee, G.; Shin, D. Enhanced Electrochemical Performance of Surface Modified $LiCoO_2$ for All-Solid-State Lithium Batteries. *Ceram. Int.* **2016**, *42*, 2140−2146.

(27) Woo, J. H.; Trevey, J. E.; Cavanagh, A. S.; Choi, Y. S.; Kim, S. C.; George, S. M.; Oh, K. H.; Lee, S.-H. Nanoscale Interface Modification of $LiCoO_2$ by Al_2O_3 Atomic Layer Deposition for Solid-State Li Batteries. *J. Electrochem. Soc.* **2012**, *159*, A1120−A1124.

(28) Ito, Y.; Otoyama, M.; Hayashi, A.; Ohtomo, T.; Tatsumisago, M. Electrochemical and Structural Evaluation for Bulk-Type All-Solid-State Batteries Using Li_4GeS_4-Li_3PS_4 Electrolyte Coating on $LiCoO_2$ Particles. *J. Power Sources* **2017**, *360*, 328−335.

(29) Sakuda, A.; Hayashi, A.; Tatsumisago, M. Interfacial Observation between $LiCoO_2$ Electrode and Li_2S-P_2S_5 Solid Electrolytes of All-Solid-State Lithium Secondary Batteries Using Transmission Electron Microscopy. *Chem. Mater.* **2010**, *22*, 949−956.

DOI: 10.1021/acsenergylett.9b01676
ACS Energy Lett. 2019, 4, 2480−2488

(30) Xiao, B.; Liu, H.; Liu, J.; Sun, Q.; Wang, B.; Kaliyappan, K.; Zhao, Y.; Banis, M. N.; Liu, Y.; Li, R.; Sham, T. K.; Botton, G. A.; Cai, M.; Sun, X. Nanoscale Manipulation of Spinel Lithium Nickel Manganese Oxide Surface by Multisite Ti Occupation as High-Performance Cathode. *Adv. Mater.* **2017**, *29*, 1703764.
(31) Lin, D.; Liu, W.; Liu, Y.; Lee, H. R.; Hsu, P.-C.; Liu, K.; Cui, Y. High Ionic Conductivity of Composite Solid Polymer Electrolyte via In Situ Synthesis of Monodispersed SiO_2 Nanospheres in Poly(ethylene oxide). *Nano Lett.* **2016**, *16*, 459−465.
(32) Li, W.; Li, M.; Hu, Y.; Lu, J.; Lushington, A.; Li, R.; Wu, T.; Sham, T.-K.; Sun, X. Synchrotron-Based X-ray Absorption Fine Structures, X-ray Diffraction, and X-ray Microscopy Techniques Applied in the Study of Lithium Secondary Batteries. *Small Methods* **2018**, *2*, 1700341.
(33) Lin, F.; Liu, Y.; Yu, X.; Cheng, L.; Singer, A.; Shpyrko, O. G.; Xin, H. L.; Tamura, N.; Tian, C.; Weng, T. C.; Yang, X. Q.; Meng, Y. S.; Nordlund, D.; Yang, W.; Doeff, M. M. Synchrotron X-ray Analytical Techniques for Studying Materials Electrochemistry in Rechargeable Batteries. *Chem. Rev.* **2017**, *117*, 13123−13186.
(34) Banis, M. N.; Yadegari, H.; Sun, Q.; Regier, T.; Boyko, T.; Zhou, J.; Yiu, Y. M.; Li, R.; Hu, Y.; Sham, T. K.; Sun, X. Revealing the Charge/Discharge Mechanism of Na-O_2 Cells by In Situ Soft X-Ray Absorption Spectroscopy. *Energy Environ. Sci.* **2018**, *11*, 2073−2077.
(35) Wang, B.; Zhao, Y.; Banis, M. N.; Sun, Q.; Adair, K. R.; Li, R.; Sham, T. K.; Sun, X. Atomic Layer Deposition of Lithium Niobium Oxides as Potential Solid-State Electrolytes for Lithium-Ion Batteries. *ACS Appl. Mater. Interfaces* **2018**, *10*, 1654−1661.
(36) Sun, Y.; Yan, W.; An, L.; Wu, B.; Zhong, K.; Yang, R. A Facile Strategy to Improve the Electrochemical Stability of a Lithium Ion Conducting $Li_{10}GeP_2S_{12}$ Solid Electrolyte. *Solid State Ionics* **2017**, *301*, 59−63.
(37) Zhao, Y.; Wu, C.; Peng, G.; Chen, X.; Yao, X.; Bai, Y.; Wu, F.; Chen, S.; Xu, X. A New Solid Polymer Electrolyte Incorporating $Li_{10}GeP_2S_{12}$ into a Polyethylene Oxide Matrix for All-Solid-State Lithium Batteries. *J. Power Sources* **2016**, *301*, 47−53.
(38) Wenzel, S.; Randau, S.; Leichtweiß, T.; Weber, D. A.; Sann, J.; Zeier, W. G.; Janek, J. Direct Observation of the Interfacial Instability of the Fast Ionic Conductor $Li_{10}GeP_2S_{12}$ at the Lithium Metal Anode. *Chem. Mater.* **2016**, *28*, 2400−2407.
(39) Haruyama, J.; Sodeyama, K.; Han, L.; Takada, K.; Tateyama, Y. Space-Charge Layer Effect at Interface between Oxide Cathode and Sulfide Electrolyte in All-Solid-State Lithium-Ion Battery. *Chem. Mater.* **2014**, *26*, 4248−4255.
(40) Ohta, N.; Takada, K.; Sakaguchi, I.; Zhang, L.; Ma, R.; Fukuda, K.; Osada, M.; Sasaki, T. $LiNbO_3$-Coated $LiCoO_2$ as Cathode Material for All Solid-State Lithium Secondary Batteries. *Electrochem. Commun.* **2007**, *9*, 1486−1490.
(41) Ohtomo, T.; Hayashi, A.; Tatsumisago, M.; Tsuchida, Y.; Hama, S.; Kawamoto, K. All-Solid-State Lithium Secondary Batteries Using the $75Li_2S{\cdot}25P_2S_5$ Glass and the $70Li_2S{\cdot}30P_2S_5$ Glass-Ceramic as Solid Electrolytes. *J. Power Sources* **2013**, *233*, 231−235.
(42) Haruyama, J.; Sodeyama, K.; Tateyama, Y. Cation Mixing Properties toward Co Diffusion at the $LiCoO_2$ Cathode/Sulfide Electrolyte Interface in a Solid-State Battery. *ACS Appl. Mater. Interfaces* **2017**, *9*, 286−292.
(43) Kondrakov, A. O.; Geßwein, H.; Galdina, K.; de Biasi, L.; Meded, V.; Filatova, E. O.; Schumacher, G.; Wenzel, W.; Hartmann, P.; Brezesinski, T.; Janek, J. Charge-Transfer-Induced Lattice Collapse in Ni-Rich NCM Cathode Materials during Delithiation. *J. Phys. Chem. C* **2017**, *121*, 24381−24388.
(44) Yu, X.; Lyu, Y.; Gu, L.; Wu, H.; Bak, S.-M.; Zhou, Y.; Amine, K.; Ehrlich, S. N.; Li, H.; Nam, K.-W.; Yang, X.-Q. Understanding the Rate Capability of High-Energy-Density Li-Rich Layered $Li_{1.2}Ni_{0.15}Co_{0.1}Mn_{0.55}O_2$ Cathode Materials. *Adv. Energy Mater.* **2014**, *4*, 1300950.
(45) Yang, J.; Muhammad, S.; Jo, M. R.; Kim, H.; Song, K.; Agyeman, D. A.; Kim, Y. I.; Yoon, W. S.; Kang, Y. M. In Situ Analyses for Ion Storage Materials. *Chem. Soc. Rev.* **2016**, *45*, 5717−5770.
(46) Li, X.; Lushington, A.; Sun, Q.; Xiao, W.; Liu, J.; Wang, B.; Ye, Y.; Nie, K.; Hu, Y.; Xiao, Q.; Li, R.; Guo, J.; Sham, T. K.; Sun, X. Safe and Durable High-Temperature Lithium-Sulfur Batteries via Molecular Layer Deposited Coating. *Nano Lett.* **2016**, *16*, 3545−3549.
(47) Yan, P.; Zheng, J.; Liu, J.; Wang, B.; Cheng, X.; Zhang, Y.; Sun, X.; Wang, C.; Zhang, J.-G. Tailoring Grain Boundary Structures and Chemistry of Ni-Rich Layered Cathodes for Enhanced Cycle Stability of Lithium-Ion Batteries. *Nat. Energy* **2018**, *3*, 600−605.
(48) Hwang, S.; Kim, S. M.; Bak, S.-M.; Kim, S. Y.; Cho, B.-W.; Chung, K. Y.; Lee, J. Y.; Stach, E. A.; Chang, W. Using Real-Time Electron Microscopy To Explore the Effects of Transition-Metal Composition on the Local Thermal Stability in Charged $Li_xNi_yMn_zCo_{1-y-z}O_2$ Cathode Materials. *Chem. Mater.* **2015**, *27*, 3927−3935.
(49) Yan, P.; Zheng, J.; Zhang, J. G.; Wang, C. Atomic Resolution Structural and Chemical Imaging Revealing the Sequential Migration of Ni, Co, and Mn upon the Battery Cycling of Layered Cathode. *Nano Lett.* **2017**, *17*, 3946−3951.
(50) Hwang, S.; Jo, E.; Chung, K. Y.; Hwang, K. S.; Kim, S. M.; Chang, W. Structural Evolution of $Li_xNi_yMn_zCo_{1-y-z}O_2$ Cathode Materials during High-Rate Charge and Discharge. *J. Phys. Chem. Lett.* **2017**, *8*, 5758−5763.
(51) Wang, M.-J.; Yu, F.-D.; Sun, G.; Wang, J.; Zhou, J.-G.; Gu, D.-M.; Wang, Z.-B. Co-Regulating the Surface and Bulk Structure of Li-Rich Layered Oxides by a Phosphor Doping Strategy for High-Energy Li-Ion Batteries. *J. Mater. Chem. A* **2019**, *7*, 8302−8314.

DOI: 10.1021/acsenergylett.9b01676
ACS Energy Lett. 2019, 4, 2480−2488